The Astrophysical Journal Letters, 938:L3 (12pp), 2022 October 10 https://doi.org/10.3847/2041-8213/ac9521

Reduced Late Bombardment on Rocky Exoplanets around M Dwarfs

Tim Lichtenberg[1,2] and Matthew S. Clement[3,4]
[1] Atmospheric, Oceanic and Planetary Physics, Department of Physics, University of Oxford, Oxford OX1 3PU, UK; lichtenberg@astro.rug.nl
[2] Kapteyn Astronomical Institute, University of Groningen, P.O. Box 800, 9700 AV Groningen, The Netherlands
[3] Earth and Planets Laboratory, Carnegie Institution for Science, Washington, DC 20015, USA
[4] Johns Hopkins APL, 11100 Johns Hopkins Road, Laurel, MD 20723, USA
Received 2022 September 6; revised 2022 September 26; accepted 2022 September 27; published 2022 October 10

Abstract

Ocean-vaporizing impacts of chemically reduced planetesimals onto the early Earth have been suggested to catalyze atmospheric production of reduced nitrogen compounds and trigger prebiotic synthesis despite an oxidized lithosphere. While geochemical evidence supports a dry, highly reduced late veneer on Earth, the composition of late-impacting debris around lower-mass stars is subject to variable volatile loss as a result of their hosts' extended pre-main-sequence phase. We perform simulations of late-stage planet formation across the M-dwarf mass spectrum to derive upper limits on reducing bombardment epochs in Hadean-analog environments. We contrast the solar system scenario with varying initial volatile distributions due to extended primordial runaway greenhouse phases on protoplanets and the desiccation of smaller planetesimals by internal radiogenic heating. We find a decreasing rate of late-accreting reducing impacts with decreasing stellar mass. Young planets around stars $\leqslant 0.4\ M_{\odot}$ experience no impacts of sufficient mass to generate prebiotically relevant concentrations of reduced atmospheric compounds once their stars have reached the main sequence. For M-dwarf planets to not exceed Earth-like concentrations of volatiles, both planetesimals, and larger protoplanets must undergo extensive devolatilization processes and can typically emerge from long-lived magma ocean phases with sufficient atmophile content to outgas secondary atmospheres. Our results suggest that transiently reducing surface conditions on young rocky exoplanets are favored around FGK stellar types relative to M dwarfs.

Unified Astronomy Thesaurus concepts: Astrobiology (74); Pre-biotic astrochemistry (2079); Exoplanet atmospheres (487); Extrasolar rocky planets (511); Planet formation (1241); Atmospheric composition (2120)

1. Introduction

Laboratory simulations of prebiotic synthesis indicate that the favored geochemical environments for the emergence of life as we know it are highly to moderately reduced (Kitadai & Maruyama 2018; Sasselov et al. 2020; Benner et al. 2020). Key precursor molecules such as hydrogen cyanide (HCN), formaldehyde (CH_2O), cyanamide (CN_2H_2), and cyanoacetylene (C_3HN) are unstable under modern Earth-like surface conditions. Thus, from a chemical point of view, the prebiotic Earth should have been a very different world than the one we inhabit today. As a result of Earth's lithosphere and crust composition being close to the quartz-fayalite-magnetite mineral buffer (Stagno & Aulbach 2021), modern volcanic emissions are dominated by oxidized gases, such as H_2O and CO_2. However, geochemical analyses of Archean and Hadean rock samples (Trail et al. 2012; Rollinson et al. 2017) suggest similar conditions on the earliest Earth, potentially the result of disproportionate ferrous and ferric iron in the mantle (Armstrong et al. 2019; Hirschmann 2022), as well as hydrogen loss from the early atmosphere (Lammer et al. 2018; Catling & Zahnle 2020; Yoshida & Kuramoto 2021).

Thus, facing a conundrum between the chemically favored environment and its apparent absence in the sampled geochemical record, recent works have turned their attention to the catalytic potential of intermittent reducing atmospheres triggered by iron-rich impactors during the tail end of Earth's accretion (Sekine et al. 2003; Hashimoto et al. 2007; Kuwahara & Sugita 2015; Genda et al. 2017a, 2017b; Schaefer & Fegley 2017; Zahnle et al. 2020; Benner et al. 2020; Itcovitz et al. 2022; Citron & Stewart 2022; Carter & Stewart 2022). Impacts of asteroidal and meteoritic materials onto Earth after the main stage of iron core formation (the "late veneer") have been used to explain the excess abundances of highly siderophile (core-affine) elements in the mantle in near-chondritic abundances (e.g., Day et al. 2016). While previously considered to be volatile rich (Albarède 2009; Halliday 2013), recent bulk elemental abundances and isotopic evidence from the inner solar system constrain the composition of this late accretion phase to be volatile poor and chemically reducing (Hirschmann 2016; Dauphas 2017; Fischer-Gödde & Kleine 2017; Carlson et al. 2018; Gillmann et al. 2020).

Phylogenetic evidence (Wolfe & Fournier 2018) and the timing of the earliest robust surface biosignatures constrain the origin of life on Earth to within the first few hundred million years after the Moon-forming impact (Pearce et al. 2018; Benner et al. 2020), suggesting that life's emergence on other rocky planets might ensue rapidly after habitable surface conditions are attained. However, more than four billion years of processing has left Earth's geological record highly biased toward younger surface ages, with the Hadean eon being only accessible via zircon inclusions (Brown et al. 2020; Korenaga 2021). These limitations make it challenging to definitively determine the timescale for triggering prebiotic synthesis within the young Earth's ambient environment, and thus motivate comparative exploration of extrasolar planets (Mojzsis 2021; Lichtenberg et al. 2022).

While G-dwarf systems hosting terrestrial planets would provide an ideal comparison to the solar system (Jontof-Hutter 2019; Wordsworth & Kreidberg 2022), their scarcity in close proximity to the Sun coupled with the limitations of the transit and radial velocity techniques greatly restrict the detailed exploration of these systems until space-based direct imaging surveys become technically viable (Apai et al. 2019; Gaudi et al. 2020; Quanz et al. 2022). However, formation models (e.g., Ogihara & Ida 2009; Miguel et al. 2011) and survey mission yields (e.g., Dressing & Charbonneau 2015; Gaidos et al. 2016) both indicate Earth-sized planets are more commonly hosted in the habitable zones of M dwarfs. While the smallest stars offer the best opportunity to study nearby Earth analogs (Scalo et al. 2007), their atmospheric and geophysical evolution may follow strongly differing trajectories due to varying volatile delivery pathways (Tian & Ida 2015; Krijt et al. 2022), the superluminous pre-main-sequence phase and flaring rates of M dwarfs (Medina et al. 2022), and the effects of tidal locking on climate (Pierrehumbert & Hammond 2019).

The best-characterized M-dwarf system to date, TRAPPIST-1, provides evidence for a break in the planetary bulk composition around the orbital runaway greenhouse threshold (Agol et al. 2021): denser inside (b, c), lighter outside (d and beyond). This can be explained by continuous water loss by photolysis from planets b and c (Luger & Barnes 2015; Wordsworth et al. 2018; Turbet et al. 2019; Dorn & Lichtenberg 2021; Barth et al. 2021). Alternatively, the density constraints may be attributed to incomplete core–mantle segregation (Elkins-Tanton & Seager 2008a) or underdense metal cores (Schlichting & Young 2022). Recent works on late-stage volatile delivery around TRAPPIST-1 and other M dwarfs suggest that water delivery from the outer disk to short-period planets is highly inefficient after nebular dispersal (Clement et al. 2022; Raymond et al. 2022) in the absence of dynamical perturbations from outer giant planets. However, admixing and migration processes during the disk phase can result in substantial, $\gtrsim$wt%-level enrichment of water and other volatile ices (Alibert & Benz 2017; Unterborn et al. 2018; Schoonenberg et al. 2019; Lichtenberg et al. 2019; Venturini et al. 2020a, 2020b; Lichtenberg & Krijt 2021). Observational evidence for volatile ice-rich (tens of wt%) super-Earths illustrate the efficacy of volatile admixing into inner planetary systems of low-mass stars (Luque & Palle 2022).

As in dynamically unperturbed G-dwarf systems, late accretion around M dwarfs is dominated by local debris. Therefore, differences in the starting configuration of protoplanets and smaller planetesimals inherited from the early formation phase may induce substantial variations in the timeline and composition of impacts. In this work, we explore the potential for rock planets around M dwarfs to experience a prolonged bombardment of dry, chemically reduced material that may induce observable epochs of transient reducing climates (Genda 2019; Rimmer et al. 2020; Ferus et al. 2020). Moreover, our models explore the consequences of varied initial conditions inherited from planetary accretion and internal geophysical and geochemical processing during the disk phase across the M-dwarf mass spectrum. We quantify (i) the rate of potentially reduced impacts large enough to trigger intermittent reduced climate states in otherwise oxidized planetary environments, and (ii) the timing of these impacts relative to the extended magma ocean epochs of M-dwarf exoplanets beyond the orbital runaway greenhouse threshold on the stellar main sequence. We outline our methods in Section 2, present and interpret our results in Sections 3 and 4, and conclude in Section 5.

2. Methods and Physical Scenarios

In this section we introduce our choice of numerical methods, starting with a description of the *N*-body simulations of the rocky-planet formation and early bombardment utilized in our analyses (reported in previous work), followed by an introduction and motivation of the initial conditions (scenarios). A more detailed discussion of the potential of prebiotic synthesis for a given planet formation and evolution scenario is presented in Section 4.

2.1. N-body Simulations and Bombardment Model

Our numerical experiments build on simulations of in situ planet formation, both in the solar system and across M dwarfs with masses 0.08–0.6 $M_{\odot}$, as reported in Clement et al. (2021, 2022). All presented *N*-body simulations use the MERCURY6 hybrid integrator (Chambers 1999) and standard settings that are commonly utilized in *N*-body studies of planet formation (e.g., surface density profile, disk mass, orbital eccentricities and inclinations of the particles, and integration time step as a fraction of the innermost particle's orbital period: Chambers 2001; Raymond et al. 2007, 2009). Other parameters such as the inner and outer radii of the terrestrial disk are necessarily scaled by stellar mass. Each of 216 total M-dwarf simulations considers a disk of 20 planetary embryos and 400 planetesimals that extends from 0.01 to 0.5 au (top panel of Figure 1). The data presented in our current investigation combine simulation outputs from models considering total disk masses of 3.0 and 6.0 $M_{\oplus}$, with the solid density decreasing with radius as $\propto r^{-3/2}$. We compare the M-dwarf models with reference models of the formation of the solar system's terrestrial planets that start with a 5.0 $M_{\oplus}$ disk of 100 embryos and 1000 planetesimals, which span the orbital range from 0.5 to 4.0 au. In order to make the most accurate comparison with the solar system possible, we choose 216 reference simulations that incorporate perturbations from the evolving giant planets (the Nice Model instability, Nesvorný & Morbidelli 2012) that have previously been tested and validated against a number of important dynamical and cosmochemical constraints (Deienno et al. 2018; Clement et al. 2019b; Mojzsis et al. 2019; Nesvorný et al. 2021).

We derive hypothetical delayed bombardment chronologies for systems with detected exoplanets in the habitable zones of host stars with masses of 0.08, 0.12, 0.4, and 1.0 $M_{\odot}$. We first select all remaining planetesimals and collisional fragments from the planet formation simulations described in Clement et al. (2019a, 2022), which includes an imperfect accretion algorithm to generate fragments. For our M-dwarf models, we combine 1375 surviving planetesimals from the original planet formation simulations with a population of 1285 collisional fragments generated by performing $\sim 10^5$ follow-on simulations of the final giant impacts in each planet formation model. We then integrate the orbital evolution of each of these massless particles (a size-frequency distribution (SFD) is added when postprocessing the simulation-derived bombardment chronologies) in several planetary systems. These include TRAPPIST-1 (Gillon et al. 2017; Agol et al. 2021), Proxima

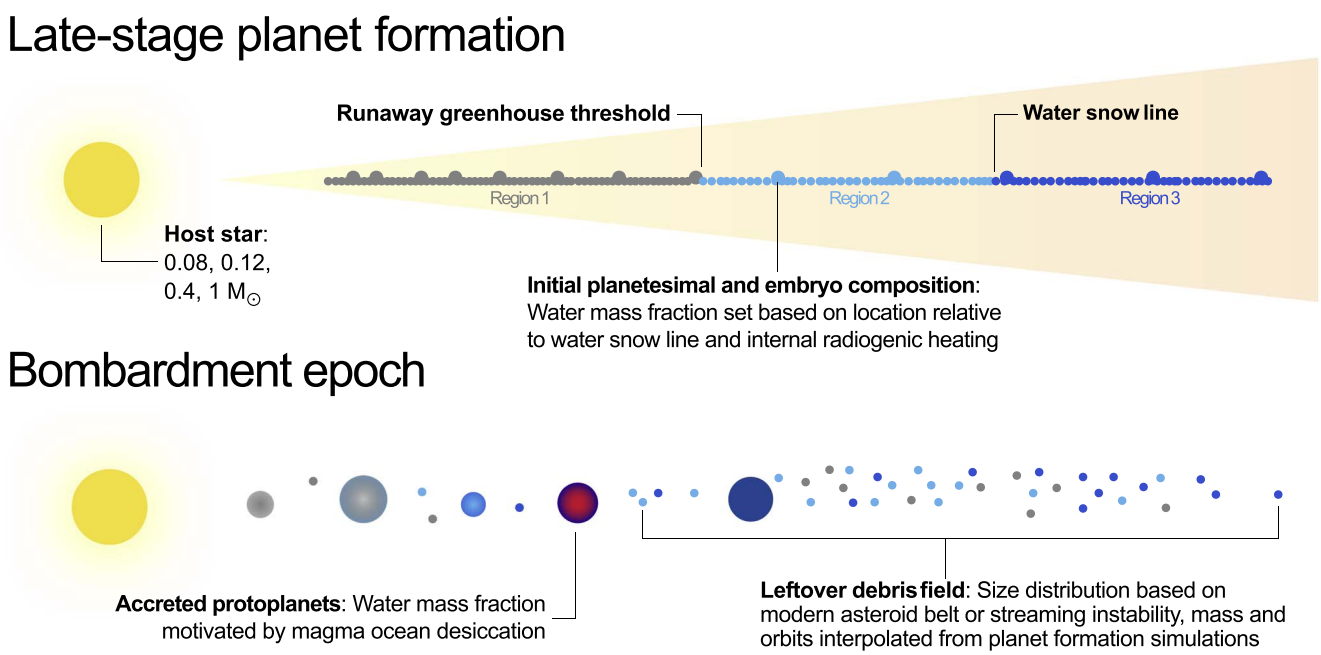

Figure 1. Illustration of the planet formation scenario incorporated in the *N*-body and long-term planetesimal bombardment simulations, described in more detail in Clement et al. (2022). Varying initial conditions related to embryo and planetesimal water content across the three regions simulate differing physical scenarios of material devolatilization and redox gradients (Lichtenberg et al. 2022) across the planetesimal disk. Scenarios are listed in Table 1 and discussed in Section 3.2.

Centauri (Damasso et al. 2020; Suárez Mascareño et al. 2020), TOI-700 (Gilbert et al. 2020; Rodriguez et al. 2020), and GJ 229 (Feng et al. 2020). To ensure the debris field spans the appropriate radial range of each system, we interpolate the semimajor axes of each particle to appropriately scale our planetesimal and fragment populations to each system of interest.

For each system, we then derive bombardment curves for the entire system, and for planetesimals and fragments originating from several radial bins at the beginning of the simulation via exponential fitting of the simulation impact chronologies. We combine these functions with the total masses of leftover material and an SFD of the debris field to generate late-impact histories for the different model systems. For all model scenarios presented in this work, we set the total mass of the leftover material to 0.1 $M_{\oplus}$, a value that is approximately equivalent to the average total mass in remaining particles at the end of our planet formation simulations and is consistent with the geochemically inferred mass of the late veneer (e.g., Raymond et al. 2013). To account for potentially different dominant accretion processes during the gas disk phase, we consider two different debris SFDs: one that is set to mimic that of the modern asteroid belt down to 1.0 km sizes, and a second analogous distribution that incorporates an additional ∼70–120 km component (20% of the total debris mass) that is motivated by the results of planetesimal formation simulations (Johansen et al. 2015; Li et al. 2019) and the sizes of main belt asteroids not belonging to collisional families (Delbo' et al. 2017).

It is worth discussing how the resolution of our models might affect our results. While modern integration algorithms (e.g., Grimm & Stadel 2014; Rein & Tamayo 2015) are capable of modeling the process of terrestrial planet formation with many more particles than utilized in our work, studies varying the number of embryos and planetesimals used have noted only minor differences in the distributions of the final systems' dynamical architectures (Clement et al. 2020; Woo et al. 2021). Thus, as the purpose of our modeling effort is to generate debris populations and study the rate of reduced impacts on potentially habitable planets, we opted to save compute time and co-add the leftover planetesimal and fragment populations from a large number of initial, lower-resolution planet formation simulations. Similarly, it is also now possible to study late bombardment more directly with high-resolution simulations. Clement et al. (2022) compared the statistical methodology described above with the results of high-resolution, GPU-accelerated bombardment simulations directly incorporating our model SFD and found the methodologies produced qualitatively similar results.

2.2. Planetesimal Composition and Impact Timing

We assess the plausible spectrum of final water mass fractions (WMFs) and bombardment histories of our models' fully formed planets in the liquid-water habitable zone via postprocessing of the planets' accretion histories. Figure 1 illustrates the compositional assumptions, and Table 1 summarizes the assumptions of 11 different disk compositional gradients that might result from disparate nebular disk thermal states and gradients during the formation (Drążkowska et al. 2022; Krijt et al. 2022) and internal evolutionary processes of planetesimals and protoplanets (Lichtenberg et al. 2022). Each model divides the disk into three different regions (Figure 1). The precise number of initial particles in each region depends on the stellar mass model used and varies between ∼4–10 embryos and ∼60–185 planetesimals. In general, models utilizing a lower stellar mass possess larger numbers of particles initially in the outermost radial bins. The first, and usually driest, region extends from the inner edge of the distribution of planet-forming material to the interior boundary of the conservative habitable zone (Region 1). We determine the inner boundary of this second region (Region 2) following Kopparapu et al. (2013), defined by the steam runaway greenhouse limit. This second orbital regime encompasses all

Table 1
Initial Water Mass Fraction (WMF) Distributions of Planetesimals and Planetary Embryos Used in the Analyses Plotted in Figure 3

Scenario		WMF Region 1		WMF Region 2		WMF Region 3	
		Embryos	Planetesimals	Embryos	Planetesimals	Embryos	Planetesimals
Solar System Reference		0.001	0.001	0.001	0.001	0.1	0.1
A	Icy 1	0.001	0.001	0.001	0.001	0.25	0.25
B	Icy 2	0.001	0.25	0.001	0.25	0.25	0.25
C	Dry 1	0.0	0.001	0.0	0.01	0.0	0.1
D	Dry 2	0.0	0.001	0.0	0.001	0.1	0.1
E	Dry 3	0.0	0.0	0.0	0.0	0.1	0.01
F	Desiccated Planetesimals 1	0.001	0.01	0.001	0.01	0.1	0.01
G	Desiccated Planetesimals 2	0.001	0.0	0.001	0.0	0.1	0.01
H	Desiccated Planetesimals 3	0.001	0.0	0.001	0.0	0.1	0.001
I	Desiccated Embryos 1	0.0	0.01	0.01	0.25	0.1	0.25
J	Desiccated Embryos 2	0.0	0.01	0.0	0.1	0.0	0.25
K	$t = 0$ Myr	0.001	0.001	0.001	0.001	0.1	0.1
	Evolve embryos $t = 1$ Myr	0.0	0.001	0.001	0.001	0.1	0.1
	$t = 10$ Myr	0.0	0.001	0.0	0.001	0.1	0.1

Note. The first column reports the model designation, and the subsequent six columns provide the initial WMF of embryos and planetesimals in Regions 1, 2, and 3 (see Figure 1). Note that, in the Evolve Embryos scenario, the disk is initialized in the same manner as in the reference case; however, after 1 Myr of simulation time, the water mass fractions of all embryos in Region 1 (including growing planets) change to 0%, and Region 2 embryos desiccate at t = 10 Myr. The physical motivation for each model scenario is discussed in Section 3.2.

of the conventional liquid-water habitable zone and stretches out to the location of the water-ice line during the evolution of the protoplanetary disk. Planetesimals and embryos in the remaining section of the disk (Region 3) are usually assigned the largest WMF values in the majority of our models. This assumes that water-rich planetesimals can easily form in Region 3 and that those objects are typically processed the least from internal radioactive heating because of time delays in planetesimal formation rates at larger orbital separations (Drążkowska et al. 2022).

The redox state of planetesimals and planetary embryos, usually measured by the FeO concentration in a sample, is crucially affected by the abundance of water, which can raise the overall oxidation state of planetary materials by reaction with other compounds (Elkins-Tanton & Seager 2008a, 2008b; Lichtenberg et al. 2022). The increased oxidation state of magmatic iron meteorites (Bonnand & Halliday 2018; Hilton et al. 2022), evidence for degassing from their parent planetesimals (Lichtenberg et al. 2021b; Hirschmann et al. 2021), fluid flow (Lewis & Jones 2016) and hydrogen incorporation (Piani et al. 2020; Jin et al. 2021) in ordinary and enstatite chondrites, accretion of water onto achondrites (Sarafian et al. 2017) and the devolatilization trend in planetary materials (Wang et al. 2019a, 2019b), both in carbonaceous and noncarbonaceous meteorites (Alexander 2019a, 2019b), all suggest a substantial initial abundance of highly volatile elements (H, C, N) in inner planetary systems during the disk phase. In addition, uncertainties in high-pressure metal-silicate partitioning allow the earliest accretion phase to be dominated by oxidized materials, fulfilling present-day constraints on Earth's mantle composition by a transition from oxidized to reduced (Siebert et al. 2013; Huang et al. 2020). This contrasts with the traditional assumption that material composition transitions from reduced to oxidized during planetary accretion (Rubie et al. 2015; O'Brien et al. 2018). Here, we use the water mass fraction before, during, and after planetesimal and protoplanet evolution as the primary marker for an object's redox state and material composition.

Following Zahnle et al. (2020) and Itcovitz et al. (2022), we are primarily interested in planetesimal impacts in the size range of ∼200–1000 km. Smaller impacts will have a substantially shorter time span of inducing transiently reducing conditions because of their limited ability to vaporize liquid-water oceans. Impacts too large, on the other hand, would melt the planetary mantle, generating a surface magma ocean and burying the planetesimal iron core in the mantle without chemically equilibrating the metal with vaporized water (Citron & Stewart 2022). The atmosphere-reducing efficacy of late-accreting debris is further dependent on the timing of the impact event. M-dwarf planetary systems undergo an extended luminous pre-main-sequence phase, during which initially water-rich or hydrogen-dominated planets undergo prolonged magma ocean phases (Schaefer et al. 2016; Lichtenberg et al. 2021a; Wordsworth & Kreidberg 2022; Barth et al. 2021; Lichtenberg et al. 2022). Prebiotically relevant impact events onto formed planets must thus happen after the runaway greenhouse transition has receded to shorter orbital distances. In addition to scrutinizing the timing of the largest events, we also calculate the total amount of water added from the leftover debris field. Through this process, we are able to derive limits beyond which surface water excesses or deficiencies of several orders of magnitude during the impact event would exclude prebiotically relevant atmospheric chemistry.

3. Results

We describe the results of our simulations here divided into two categories. In Section 3.1, we focus solely on the timing

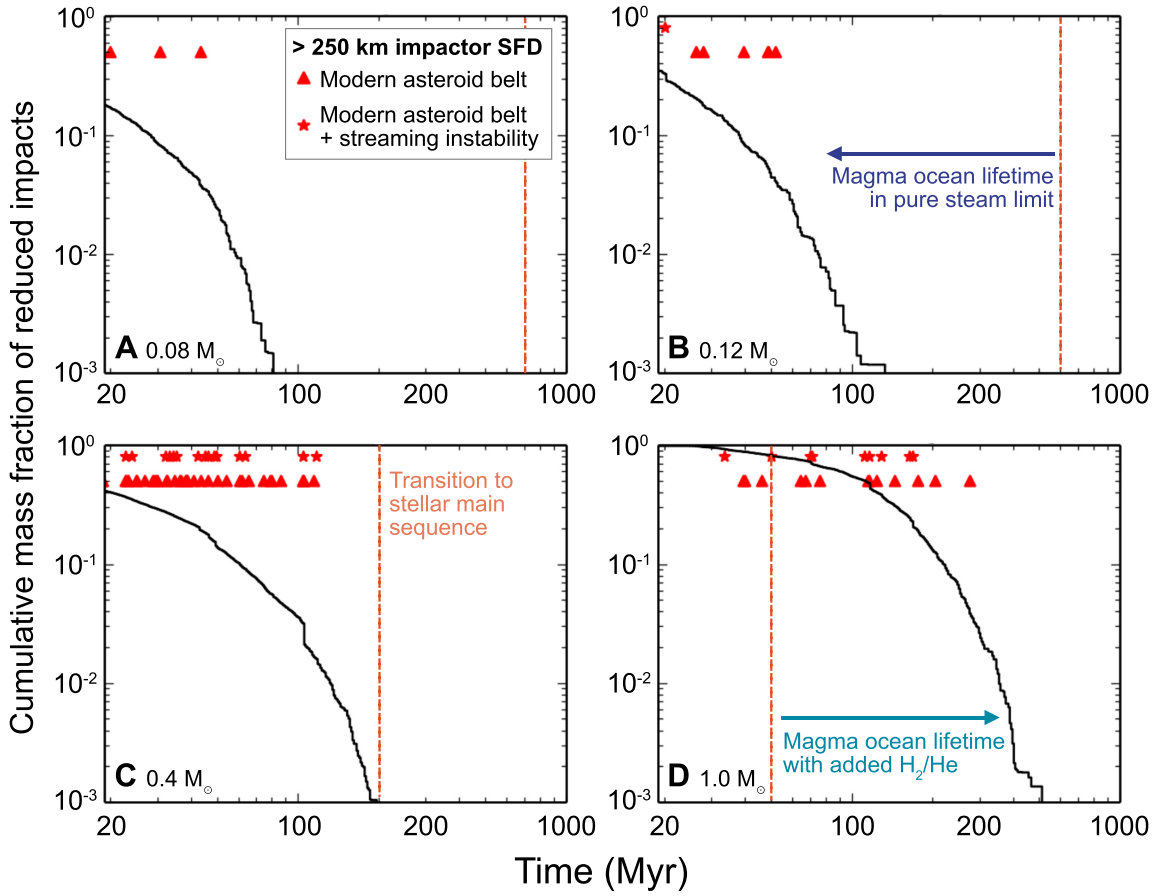

Figure 2. Timing of reduced impacts onto potentially habitable exoplanets around stars of variable mass (panels (A)–(D)). The black lines illustrate the (inverse) cumulative debris mass fraction over time sourced from inside the water snow line. Red symbols indicate the timing of impact events larger than 250 km in diameter, an approximate efficacy threshold to trigger intermittent reduced climate states. Triangle symbols represent cases where the leftover debris field is sourced from an SFD comparable to the modern asteroid belt. Star symbols include an additional 5% of 80–130 km objects, similar to the peak of the birth planetesimal population generated by the streaming instability. Orange vertical lines demarcate the arrival of the star in each scenario onto the main sequence. In the pure steam limit (water-dominated atmospheres), the magma ocean lifetime can be shorter than this (blue arrow in B); in scenarios with substantial primordial H_2/He atmospheres (green arrow in D), the magma ocean lifetime is enhanced. Only for G dwarfs, such as the Sun, do appreciable quantities of late bombardment hit potentially habitable planets beyond the pre-main-sequence phase.

and intervals of bombardment episodes, while in Section 3.2, we present the influence of the different chemical scenarios on the composition of the late-stage bombardment and resulting planets.

3.1. Timing of Impacts

Figure 2 illustrates the timing of the arrival of late-impacting debris onto planets beyond the runaway greenhouse transition, in potentially habitable orbits, after the initial magma ocean phase. For cases 0.08 $M_\odot$ (panel (A)), 0.12 $M_\odot$ (panel (B)), and 0.4 $M_\odot$ (panel (C)), bombardment is focused on the pre-main-sequence phase (orange dashed transition timings from Baraffe et al. 2015). Specifically for lower-mass M dwarfs, late impacts cease at around 100 Myr. Only a handful of impacts are massive enough to potentially induce prebiotically relevant reduced climate states. For 0.4 $M_\odot$ (panel (C)), the end of the bombardment epoch coincides approximately with the transition to the main sequence, and the amount of larger impacts increases substantially. However, such impacts predominately occur in the first ∼100–150 Myr after system formation. For solar-type stars, 1.0 $M_\odot$ (panel (D)), the bombardment epoch extends to about 300–400 Myr while the main-sequence transition is shifted to much earlier times (≈50 Myr). This means that for G dwarfs, more than 80% of debris arrives during the stellar main sequence. Impacts of large objects on G stars continue until about 200–300 Myr after system formation.

3.2. Volatile Delivery across Physical Scenarios

Figure 3 shows our results for the delivery of water—and hence oxidizing power—during the bombardment phase of M- and G-dwarf planetary systems. We subdivide the results into various classes of scenarios: a solar system reference case, two end-member scenarios of initially very volatile-rich (Icy) and volatile-poor (Dry) systems, and intermediate scenarios that account for radioactive heating of small planetesimals (Desiccated Planetesimals) and magma ocean desiccation (Desiccated Embryos) in isolation, while (Evolve Embryos) additionally accounting for the time sequence of volatile loss by photolysis from molten protoplanets. We discuss the physical motivation for each model and the results of the respective bombardment simulations below.

Solar System Reference—The solar system reference scenario illustrates the dynamical and compositional case of the solar system after the gas disk phase: relatively dry, volatile-poor (0.001 wt%) bodies inside the asteroid belt (Alexander 2019a; Jin & Bose 2019; Piani et al. 2020;

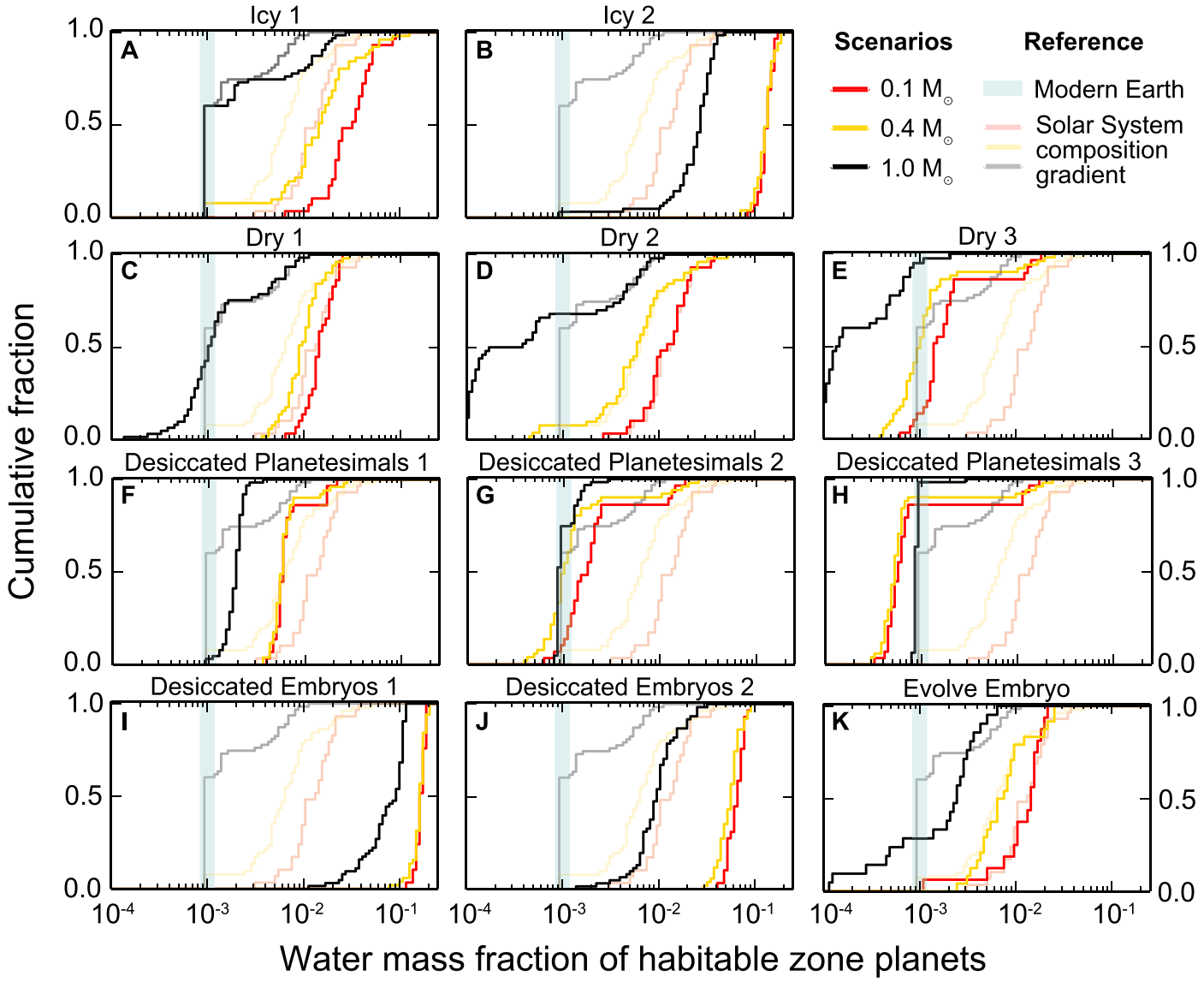

Figure 3. Water mass fraction distribution across the model scenarios (panels (A) to (K)) in Table 1 for 0.1 (red), 0.4 (yellow), and 1.0 (black) $M_{\odot}$ stars with the fiducial solar system composition gradient (light gray, yellow, and red lines) as reference cases. The modern Earth water mass fraction with uncertainties is indicated as a light blue-green band. The physical motivation for each model scenario is discussed in Section 3.2. Across most scenarios, M-dwarf exoplanets receive orders of magnitude more water than the modern Earth. Earth-like WMFs for M-dwarf exoplanets are produced with >50% probability for scenarios Dry 3 (panel (E)) and Desiccated Planetesimals 3 (panel (H)).

Stephant et al. 2021; Jin et al. 2021), and somewhat wetter but volatile depleted (0.1 wt%) outside. Carbonaceous asteroids hosting a few wt% of water on average (Alexander et al. 2018; Alexander 2019b) motivate our outer compositions. These inferred bulk abundances of water and other volatile ices (Kurokawa et al. 2022; Krijt et al. 2022) relative to the primordial, disk-inherited compositions (closer to that of comets: $\gtrsim$25 wt%) represent the combined influence of internal radiogenic heating (Bland & Travis 2017; Lichtenberg et al. 2021b) and collisional overprinting. The dynamical configuration of small bodies in the solar system was also sculpted by stochastic scattering events with the giant planets, which transports a significant amount of volatile-rich debris toward the inner solar system, enriching the terrestrial planets during the end phase of planetary accretion (Raymond & Izidoro 2017; Deienno et al. 2022). In the solar system reference scenario (Figure 3, gray line), about 60% of planets accrete Earth-like abundances of volatiles (the local baseline), with the upper $\approx$30%–40% still within the upper limit of Earth's water bulk abundance (Peslier et al. 2017).

Icy (A/B)—The Icy scenarios assume that—unlike in the solar system—internal heating from short-lived radioactive elements like ^{26}Al is significantly reduced and that magma ocean desiccation during the pre-main-sequence phase does not operate. Volatile ice abundances in planetesimals are thus set by the local disk chemistry (Öberg & Bergin 2021; Miotello et al. 2022). Icy 1 assumes that internal radioactive heating in planetesimals was comparable in Region 1 and Region 2, but nonexistent beyond the snow line, either due to inhomogeneous enrichment (higher abundances of ^{26}Al in the inner disk; Adams 2021) or slower planetesimal formation and hence reduced heating in the outer disk (Drążkowska & Dullemond 2018; Charnoz et al. 2021). In this situation, planets in the 1.0 $M_{\odot}$ simulation accrete somewhat more water from the outside-in scattering of Region 3 planetesimals. In contrast, the M-dwarf simulations accrete significantly more water, between

0.01 and 0.1 wt, one to two orders of magnitudes above Earth's value. In Icy 2, planetesimals in Region 1/2 are also ice rich. This corresponds to a scenario where planetesimal formation generally occurs at the outward- (during the Class I stage) and then inward-moving (Class II stage) density jump across the water snow line (Schoonenberg & Ormel 2017; Drążkowska & Alibert 2017) while the disks forms and in the absence of radioactive heating. In this case, the M-dwarf simulations sample near-maximum abundances of water throughout, between 0.1–0.2 wt, while the G-dwarf planets reach between 0.01–0.1 wt on average.

Dry (C/D/E)—The Dry scenarios assume that both desiccation by magma ocean losses and internal radiogenic heating of planetesimals are operating to various degrees of efficacy. In Dry 1, protoplanets completely desiccate from magma ocean losses and planetesimals dehydrate with decreasing efficacy from Region 1 to Region 3 due to slower planetesimal formation with increasing distance (or, alternatively, higher ^{26}Al in the inner disk). In Dry 2, planetesimal dehydration in Region 2 is enhanced from 0.01 to 0.001 relative to Dry 1. In both scenarios, M-dwarf planets receive on average about 0.01 wt water, while G-dwarf planets are drier: about 50% above Earth levels for Dry 1 and about 40% above Earth for Dry 2. However, Dry 2 forms much drier planets on average, down to about 0.0001 wt planets for the most volatile-depleted simulations. The Dry 3 setting increases planetesimal dehydration further, such that G-dwarf planets barely reach Earth-like water levels, while M-dwarf planets now accrete to approximately Earth-like levels through late-stage debris.

Desiccated Planetesimals (F/G/H)—This scenario fixes magma ocean losses and increases planetesimal dehydration via radioactive heating by region (inside-out) and total magnitude. For the G-star simulations, the effects from changes in the initial planetesimal water mass fractions are minor across our range of tested scenarios, such that the difference between Desiccated Planetesimals 1 and Desiccated Planetesimals 3 results in the statistical dehydration of rocky planets between about 2–3 times. For the M-star simulations, however, the increasing dehydration from Desiccated Planetesimals 1 to Desiccated Planetesimals 3 is stark, resulting in a shift from about 0.01 wt water levels for Desiccated Planetesimals 1 to about 80% of planets being drier than Earth for Desiccated Planetesimals 3. This illustrates the strong effect of early volatile loss by internal radioactive heating of planetesimals during the late-stage bombardment episode of rocky-planet formation.

Desiccated Embryos (I/J)—These scenario setups pose the general question of whether magma ocean water losses can outcompete planetesimal dehydration to achieve Earth-similar water mass fractions for rocky planets in potentially habitable orbits by increasing the loss levels for embryos. In Desiccated Embryos 1, embryo water mass fractions decrease from 0.1 wt in Region 3 to 0.0 wt in Region 1. This assumes that the timescale the planets spend inside the orbital runaway greenhouse threshold is a major factor in desiccation efficacy (Schaefer et al. 2016; Wordsworth et al. 2018) and that the small planetesimals in Region 2 and Region 3 are primitive, icy, and unaffected by radioactive heating. These simulations produce water mass fractions on the order of 0.1 wt, about two to three orders of magnitude above Earth's levels. In Desiccated Embryos 2, all embryos are completely dried out from magma ocean loss effects, and the planetesimals' water mass fraction in Region 2 is reduced. In this situation, G-star planets achieve on the order of 0.01 wt and M-star planets receive on the order of 0.05–0.1 wt of water—one to two orders of magnitude above Earth's water mass fraction.

Evolve Embryo (K)—This scenario assumes that planetesimal internal heating is comparable to the solar system and magma ocean losses are time dependent for the first 10 Myr after system formation, when pre-main-sequence stars peak in luminosity. In this scenario, about 25% of the G-star simulations become drier than Earth, while 75% end up being up to one order of magnitude more water rich ($\leqslant$0.01 wt). M-star simulations reach about 0.005–0.03 wt on average—an order of magnitude above Earth's water levels.

4. Discussion

4.1. Impact-generated Reduced Climate States on Exoplanets

Our bombardment simulations suggest that the late-stage delivery of reducing power via iron-rich impacts in M-dwarf systems is (i) statistically rare and (ii) likely not capable of triggering intermittent reducing climates at all. Because the leftover debris mass in M-dwarf systems after the main formation era is already heavily depleted compared to G-star systems, late-stage impacts are focused on earlier times (Figure 2). Late-stage impacts acting as a deus ex machina for subaerial prebiotic chemistry in M-dwarf systems are potentially problematic on two accounts. First, the impact flux peaks at very early times, which is likely too early for impacts to play a major role in resetting atmospheric chemistry. If an iron-rich impactor strikes an already reduced atmosphere, the timescale of opportunity (Zahnle & Carlson 2020) is not simply multiplied because the atmospheric reduction in the scenario is dependent on the presence of a surface ocean, which is related to the total mass budget of liquid water at the surface. Second, the arrival of the most massive impactors, which are the most effective in triggering extended reduced atmospheres by equilibrating with sufficient surface water, is limited to a few tens of Myr in M-star systems. At this time, the runaway greenhouse threshold is far outside the orbit of planets that reside in potentially habitable regions during the stellar main-sequence phase (Luger & Barnes 2015; Schaefer et al. 2016), meaning they will be in a global magma ocean regime (Wordsworth & Kreidberg 2022; Lichtenberg et al. 2022) because a fraction of an Earth's ocean mass is already sufficient to keep the planetary surface temperature above the melting temperature of rocks (Boukrouche et al. 2021). If the planetary mantle is a magma ocean, impactor iron merges with the target body core (Kendall & Melosh 2016).

This outcome is focused on M dwarfs due to their luminous pre-main-sequence phase. G-dwarf planets, on the other hand, experience numerous large impacts over an extended time period of hundreds of Myr. If the solar system is typical in its inner-system composition, then G-dwarf exoplanets may undergo similar bombardment episodes during the tail end of accretion. However, as our simulations across different compositional setups (Figure 3) demonstrate, this conclusion is sensitively dependent on the mechanism of dehydration.

While recent work suggests that even G-dwarf exoplanets can undergo major shifts in their atmospheric composition during their magma ocean epoch (Wordsworth et al. 2018; Krissansen-Totton et al. 2021), unlike planets inside the runaway greenhouse threshold (Hamano et al. 2015;

Massol et al. 2016; Ikoma et al. 2018), G-dwarf planets in the liquid-water habitable zones of their stars will not desiccate to completion. Because rocky planets in this case can solidify efficiently, ocean formation timescales (Salvador et al. 2017) are shorter than the average time interval between subsequent large impactors, thus maximizing the influence of each individual impactor per unit mass. The SFD of impacting debris contributes to this conclusion. A distribution similar to the modern asteroid belt achieves massive impacts throughout all planetary systems, including the M-dwarf mass spectrum down to 0.1 $M_{\odot}$. In this mass domain, no massive impacts at all are generated if the SFD incorporates an increasing fraction of birth planetesimals formed through streaming instability (see Figure 2). This suggests that collisional and secondary processing during planetary accretion tend to extend the timescale for late-accreting debris (Morbidelli et al. 2009; Quintana et al. 2016).

So far we have solely analyzed the timing of impacts, but what about their composition? For impacts to catalyze the atmospheric production of reduced nitrogen compounds, the impactor itself has to be reduced. In the solar system, only a few known meteorites (for instance, enstatite chondrites or aubrite achondrites) are expected to feature compositions that would allow this. All other known meteorite classes—even magmatic irons and H chondrites—overlap with carbonaceous chondrites in their whole-body oxidation states (Bonnand & Halliday 2018; Hilton et al. 2022; Corrigan et al. 2022). This contrasts with the standard assumption in the literature that the inner and outer solar system compositions are solely caused by the location of the water snow line during the disk phase (O'Brien et al. 2018), motivating alternative redox and thermal trajectories for the inner solar system planetesimal population (Grimm & McSween 1993; Siebert et al. 2013; Alexander 2019a; Huang et al. 2020; Lichtenberg et al. 2021b). The uncertainty on the earliest geophysical evolution of the inner solar system planetesimal population is underlined by recent evidence for the fractionation of refractory and moderately volatile elements (Norris & Wood 2017; Hin et al. 2017), which suggests that the terrestrial planet-forming planetesimals experienced significant melting and vaporization at least partially caused by internal heating from short-lived radioactive isotopes (Young et al. 2019; Benedikt et al. 2020). If the present-day composition of inner solar system planetesimals is inherited from prior redox evolution, the consequences for atmospheric diversity among the rocky exoplanet population may be profound (Lichtenberg et al. 2019; Lichtenberg & Krijt 2021; Krijt et al. 2022), as further illustrated by our late-stage bombardment simulations. Taking the water mass fraction of planetesimals as a proxy for the whole-body oxidation state, only simulations that substantially dehydrate from internal radioactive heating experience any late-stage impacts of reduced debris. This suggests that reduced climates on rocky exoplanets around M dwarfs are unlikely to be caused by bombardment. Therefore, internal geophysical and geochemical processes to escape planetary self-oxidation (Gaillard et al. 2021), such as rain-out quenched magma ocean regimes (Lichtenberg 2021), may instead enable long-lived outgassed atmospheres rich in reduced compounds (Liggins et al. 2020, 2022). Alternatively, HCN (Todd & Oberg 2020) or prebiotic organics (Paschek et al. 2021, 2022) may be synthesized inside the planetesimals and delivered directly with the impact.

4.2. Late-stage Volatile Delivery in M-dwarf Systems

While aimed at providing insight into the likelihood of reduced impacts on rocky exoplanets, our simulations also provide a different viewing angle on the volatile delivery around smaller stars. While late-stage impact bombardment in the solar system previously had been assumed to be volatile rich, the highly siderophile element concentrations in Earth's lithosphere require the so-called late veneer to be dominated by dry, reduced material (Day et al. 2016; Kleine & Walker 2017; Dauphas 2017; Carlson et al. 2018). Given the results of our simulations and the accompanying discussion in the previous subsection, this conclusion directly translates into consequences for the volatile abundance in extrasolar planets. All but the driest of bombardment simulations yield a significant (up to several orders of magnitude) overabundance of water relative to the terrestrial planet population. In the context of sub-Neptunes, Bean et al. (2021) argued that dry planets can be formed by protoplanets accreting locally and growing from an influx of abundant dry pebbles inside the water snow line (their "drift" end-member scenario). This would provide a physical mechanism for the currently dominant explanation for the Kepler radius valley (Fulton et al. 2017): escape of primordial H_2/He from otherwise volatile-poor cores (Owen & Wu 2017; Ginzburg et al. 2018; Rogers & Owen 2021). However, models invoking the migration of protoplanets (Venturini et al. 2020a, 2020b) and of the water snow line (Sasselov & Lecar 2000; Drążkowska & Dullemond 2018) during the disk phase suggest otherwise, for which increasing observational evidence around M-dwarf stars is found (Luque & Palle 2022).

Our simulation results indicate that, even if protoplanets were to escape the main accretion era dominantly dry, they would receive an abundant influx of late-accreting volatile-rich debris. This influx is high enough to overcompensate even the largest atmospheric escape fluxes predicted for ultrashort-period exoplanets. For example, Bourrier et al. (2018) estimated the maximum water mass to escape from 55 Cancri —a highly irradiated super-Earth—to be ≈100 Earth oceans, and more likely in the range of a few to a few tens of Earth oceans. Similarly, Luger & Barnes (2015) and Wordsworth et al. (2018) find total escape fluxes to be limited to a few tens of Earth oceans for a wide range of irradiation environments and planetary masses. In our simulations, only the Desiccated Planetesimals scenarios achieve water mass fractions low enough for atmospheric escape to strip the planets completely of their water contents. This is because high mean molar mass compounds such as water are hard to drive off a planet in the quantities our delivery simulations suggest (Lammer et al. 2018; Owen et al. 2020). Similarly, the water mass fractions derived from our simulations are too large to be efficiently eroded by the drier impacts (Sinclair et al. 2020; Gillmann et al. 2020). The suggestion of a substantial influx of late volatiles from local and farther out debris shares some similarities with the hypothesis of atmospheric rejuvenation by exocomets from extrasolar debris disks (Kral et al. 2018; Wyatt 2020). However, because rocky planets in M-dwarf systems likely undergo long-lived magma ocean phases—as outlined above—most of these volatiles will be dissolved in the magma ocean and stored in the mantle (Dorn & Lichtenberg 2021). This lowers escape rates relative to the assumption that all volatiles are stored on the surface and can potentially explain the origin of the density dichotomy of the TRAPPIST-1 system

(Turbet et al. 2019; Agol et al. 2021) and the density distribution in the K2-3 system (Diamond-Lowe et al. 2022).

4.3. Caveats

Our simulations explore the impact of varying physical devolatilization mechanisms in M-dwarf planetary systems by use of different scenarios that vary the water mass fraction, stellar mass, and planetesimal distribution. Water loss via photolysis from magma oceans, however, operates on timescales comparable to the pre-main-sequence evolution of M dwarfs. Therefore, a more refined treatment of magma ocean evolution in conjunction with planet formation and bombardment simulations is required in order to predict detailed compositions for individual systems—as will be necessary for the exploration of individual planets in the JWST era.

Our *N*-body models necessarily assume that all habitable zone planets around M dwarfs formed via giant impacts in the same manner as the solar system's terrestrial planets. Thus, our study does not incorporate a wide sweep of potential initial conditions that may arise if the role of pebble accretion is greater than in the solar system. This may shift our estimates to lower impact rates, and we therefore regard our results as upper limit estimates on the rate of late impacts. However, it is reasonable to argue that debris-producing giant impacts occur in most rocky-planet formation scenarios (see further discussion in Clement et al. 2022), even if the majority of planet growth occurred via pebble accretion rather than direct planetesimal–planetesimal growth. It is also important to note that a range of dynamical formation models currently purports to explain the origin of the inner solar system (e.g., Raymond et al. 2020). Worse still, different potentially viable evolutionary scenarios for the terrestrial planets yield disparate late bombardment chronologies (Clement et al. 2019a), and it remains challenging to constrain models in this manner by inferring an impact history from crater counts on terrestrial bodies (e.g., Evans et al. 2018; Brasser et al. 2020). Thus, any attempt to neatly map solar system science to the exoplanet regime should be viewed with a degree of skepticism. Therefore, our study should be viewed more as an exploration of the range of plausible end states, rather than a definitive model for any particular system.

Finally, throughout this work, we use water mass fraction as a proxy for the oxidation state. However, the impact of various loss mechanisms such as dehydration by short-lived radionuclides can fractionate the material redox state from the water mass fraction. For instance, this may happen via serpentinization processes on planetesimals during internal heating. Further work is required to quantify the redox evolution during the internal geophysical and geochemical evolution of planetesimals, both in the solar system and in extrasolar planetary systems.

4.4. Observational Tests

Our numerical experiments suggest that M-dwarf exoplanets—and any surviving debris—should be water rich and oxidized. This is testable using astronomical observations of both individual exoplanets and from statistical correlations via survey missions such as TESS and PLATO. On a statistical level, evolution is dominated by two effects: (i) desiccation via internal heating on planetesimals and (ii) magma ocean losses on protoplanets. The former operates on a system level at early stages (Lichtenberg et al. 2019; Lichtenberg & Krijt 2021), while the latter operates to different degrees over time and is sensitive to irradiation (Schaefer et al. 2016; Lichtenberg et al. 2022).

If M-dwarf planetary systems in fact feature late impacts of reducing debris—as is realized in a minor fraction of our simulations only—then JWST may be able to observe the transient signature of this (Ferus et al. 2020; Rimmer et al. 2021). Our simulations predict the observable time window for this to be in the first few tens of Myr across the M-dwarf mass spectrum. However, in such a case, the observation would need to take into account the underlying magma ocean. Distinguishing between a reduced magma ocean scenario (Lichtenberg 2021; Schlichting & Young 2022) and an impact-induced reduced atmosphere (Rimmer et al. 2020) may require observations in the near- to mid-infrared to differentiate the near-surface temperature (Lichtenberg et al. 2021a). The dense sub-Earth GJ 367b (Lam et al. 2021) may provide an attractive observational target, if its host star is within the first ∼100 Myr of its life, as suggested by Brandner et al. (2022).

Finally, observational evidence from polluted white dwarfs suggests a fraction of the observed debris is core or mantle material (hence, the debris from differentiated planetesimals; Bonsor et al. 2020), while others demonstrate evidence for water-rich compositions (Raddi et al. 2015; Doyle et al. 2021). Finding the source of these compositional trends will help to refine predictions for exoplanetary systems and the probability of reduced versus oxidized (and volatile-rich) late bombardment (Bonsor et al. 2020; Curry et al. 2022).

5. Summary and Conclusions

We performed late-stage impact bombardment simulations with a focus on rocky exoplanets in the liquid-water habitable zones of M stars between 0.1 and 0.4 $M_{\odot}$ with the goal of quantifying the chances of triggering transiently reducing conditions suitable for subaerial prebiotic chemistry in Hadean Earth analog environments. In order to test different initial planetary embryo and planetesimal compositions, we subdivided the disk into three regions, corresponding to inside (Region 1) and outside (Region 2) the steam runaway greenhouse limit, and outside the water snow line (Region 3). Impact bombardment curves are derived based on two initial SFDs, based on the modern asteroid belt and one including an additional contribution of planetesimals akin to the outcome of the streaming instability.

The compositions of planetary embryos and planetesimals in each bombardment scenario are initiated with a different water mass fraction, which we take as a first-order proxy for the redox state. The water mass fraction of planetary embryos is assumed to be influenced by the orbit of the water snow line during the formation of the initial planetesimal swarm that formed the embryo and water loss due to photolysis during primordial runaway greenhouse (magma ocean) episodes of the extended preluminous main-sequence phase of M stars. Initial planetesimal compositions are assumed to be influenced by orbital location relative to the water snow line and dehydration based on internal heating by short-lived radioactive isotopes such as ^{26}Al. Overall, we compare five different general settings, varying the radial and temporal distribution of water mass fractions in embryos and planetesimals across the M-dwarf mass spectrum, which simulates different degrees of magma ocean desiccation, planetesimal dehydration, and

planetesimal formation timescale relative to the radial evolution of the water snow line.

Summarizing our results, we find:

1. The majority of bombardment epochs in our simulations are dominated by water-rich compositions, comparable to carbonaceous chondrite-like or cometary compositions, and hence oxidizing in bulk abundance, in contrast to the composition of the late veneer in the solar system. Only the simulations that are set up to simulate the driest-possible end-member cases (Dry 3 and Desiccated Planetesimals 3) achieve planetary bombardment episodes that include dry and hence reducing impacts that could conceivably trigger intermittent reducing climate states amenable for subaerial prebiotic chemistry. A late veneer-analog bombardment of chemically reduced planetesimals that deliver reducing power in the form of iron metal to react with vaporized oceans is thus only possible when planetesimals dehydrate substantially relative to their primordial, disk-derived compositions.
2. Across the entire M-dwarf mass spectrum, the late-stage bombardment of young rocky planets ceases before the star transitions onto the main sequence. Young exoplanets that incorporate H_2O or H_2 abundances comparable to the early Earth—as suggested by the density dichotomy between the super-Earth and sub-Neptune regimes and our planet formation simulations—will be covered by global primordial magma oceans during this time window. Therefore, all late-stage debris will fall into the magma ocean without being able to chemically equilibrate with surface water.
3. Integrated over all possible volatile delivery scenarios, we find the total bulk abundances of M-dwarf exoplanets to be strongly volatile enriched compared to those of the solar system's terrestrial planets. Based on previous estimates of atmospheric escape fluxes and the longevity of magma ocean episodes under strong irradiation, this suggests that M-dwarf exoplanets typically escape their primordial runaway greenhouse phases with sufficient bulk atmophile content to regenerate secondary atmospheres via outgassing from their mantle reservoir. From a compositional perspective, M-dwarf exoplanets with irradiation levels comparable to the modern Earth are not in danger of losing their atmospheres. Rather, the challenge is to get rid of an overabundance of volatiles to enable a potentially habitable surface.
4. Solar-like planetary systems therefore are statistically more likely to experience intermittent reduced climate states early in their evolution—a key requirement to initiate prebiotic synthesis in the subaerial origin of life scenarios. In the absence of chemically reducing processes, such as incomplete core–mantle differentiation in super-Earths, this suggests that M-dwarf rocky exoplanets might host oxidizing atmospheres and feature substantially decreased bulk densities relative to an Earth-like composition.
5. In contrast, G-dwarf stars experience late-stage impacts for hundreds of millions of years after rocky planets in their liquid-water habitable zones have solidified. In addition, G-dwarf planetary systems generally receive drier late-stage impacts than M-dwarf exoplanets. On average, the final bulk water abundances of G-star exoplanets are between one to two orders of magnitude lower compared to those of M-dwarf exoplanets.

Our results highlight the intimate connection between compositional variables set by early disk chemistry, geophysical internal processes, and dynamical planet formation scenarios that can affect the long-term atmospheric content and surface conditions of rocky exoplanets. Our simulations offer predictions that are testable via atmospheric and surface observations of short-period exoplanets in M-dwarf planetary systems and compositional analyses of debris disks and polluted white dwarfs. Combining insights from the geophysical exploration of young, Hadean-analog exoplanets and the distribution of climate states across the rocky exoplanet census will enable a sharper picture of plausible prebiotic environments and pathways to the origin of life as we know it on our own world.

The authors are grateful for useful discussions with Anat Shahar and Nick Wogan, as well as the constructive report of an anonymous reviewer. The work described in this manuscript was supported by the AEThER project, funded by the Alfred P. Sloan Foundation under grant No. G202114194, the Simons Foundation (SCOL Award No. 611576), Carnegie Science's Scientific Computing Committee for High-Performance Computing (hpc.carnegiescience.edu), and benefited from information exchange within the program 'Alien Earths' (NASA Grant No. 80NSSC21K0593) for NASA's Nexus for Exoplanet System Science (NExSS) research coordination network. This work also used the Extreme Science and Engineering Discovery Environment (XSEDE), which is supported by National Science Foundation grant No. ACI-1548562. Specifically, it used the Comet system at the San Diego Supercomputing Center (SDSC). This research made use of resources provided by the Open Science Grid (Pordes et al. 2007; Sfiligoi et al. 2009), which is supported by the National Science Foundation Award No. 1148698, and the US Department of Energy's Office of Science. Some of the computing for this project was performed at the University of Oklahoma's Supercomputing Center for Education and Research (OSCER).

ORCID iDs

Tim Lichtenberg https://orcid.org/0000-0002-3286-7683
Matthew S. Clement https://orcid.org/0000-0001-8933-6878

References

Adams, F. C. 2021, ApJ, 919, 10
Agol, E., Dorn, C., Grimm, S. L., et al. 2021, PSJ, 2, 1
Albarède, F. 2009, Natur, 461, 1227
Alexander, C. M. O. 2019a, GeoCoA, 254, 246
Alexander, C. M. O. 2019b, GeoCoA, 254, 277
Alexander, C. M. O., McKeegan, K. D., & Altwegg, K. 2018, SSRv, 214, 36
Alibert, Y., & Benz, W. 2017, A&A, 598, L5
Apai, D., Milster, T. D., Kim, D. W., et al. 2019, AJ, 158, 83
Armstrong, K., Frost, D. J., McCammon, C. A., Rubie, D. C., & Boffa Ballaran, T. 2019, Sci, 365, 903
Baraffe, I., Homeier, D., Allard, F., & Chabrier, G. 2015, A&A, 577, A42
Barth, P., Carone, L., Barnes, R., et al. 2021, AsBio, 21, 1325
Bean, J. L., Raymond, S. N., & Owen, J. E. 2021, JGRE, 126, e06639
Benedikt, M. R., Scherf, M., Lammer, H., et al. 2020, Icar, 347, 113772
Benner, S. A., Bell, E. A., Biondi, E., et al. 2020, ChemSystemsChem, 2, e1900035
Bland, P. A., & Travis, B. J. 2017, SciA, 3, e1602514
Bonnand, P., & Halliday, A. N. 2018, NatGe, 11, 401

Bonsor, A., Carter, P. J., Hollands, M., et al. 2020, MNRAS, 492, 2683
Boukrouche, R., Lichtenberg, T., & Pierrehumbert, R. T. 2021, ApJ, 919, 130
Bourrier, V., Dumusque, X., Dorn, C., et al. 2018, A&A, 619, A1
Brandner, W., Calissendorff, P., Frankel, N., & Cantalloube, F. 2022, MNRAS, 513, 661
Brasser, R., Werner, S. C., & Mojzsis, S. J. 2020, Icar, 338, 113514
Brown, M., Johnson, T., & Gardiner, N. J. 2020, AREPS, 48, 291
Carlson, R. W., Brasser, R., Yin, Q.-Z., Fischer-Gödde, M., & Qin, L. 2018, SSRv, 214, 121
Carter, P. J., & Stewart, S. T. 2022, PSJ, 3, 83
Catling, D. C., & Zahnle, K. J. 2020, SciA, 6, eaax1420
Chambers, J. E. 1999, MNRAS, 304, 793
Chambers, J. E. 2001, Icar, 152, 205
Charnoz, S., Avice, G., Hyodo, R., Pignatale, F. C., & Chaussidon, M. 2021, A&A, 652, A35
Citron, R. I., & Stewart, S. T. 2022, PSJ, 3, 116
Clement, M. S., Kaib, N. A., & Chambers, J. E. 2020, PSJ, 1, 18
Clement, M. S., Kaib, N. A., Raymond, S. N., & Chambers, J. E. 2021, Icar, 367, 114585
Clement, M. S., Kaib, N. A., Raymond, S. N., Chambers, J. E., & Walsh, K. J. 2019a, Icar, 321, 778
Clement, M. S., Quintana, E. V., & Quarles, B. L. 2022, ApJ, 928, 91
Clement, M. S., Raymond, S. N., & Kaib, N. A. 2019b, AJ, 157, 38
Corrigan, C. M., Nagashima, K., Hilton, C., et al. 2022, GeCoA, 333, 1
Curry, A., Bonsor, A., Lichtenberg, T., & Shorttle, O. 2022, MNRAS, 515, 395
Damasso, M., Del Sordo, F., Anglada-Escudé, G., et al. 2020, SciA, 6, eaax7467
Dauphas, N. 2017, Natur, 541, 521
Day, J. M. D., Brandon, A. D., & Walker, R. J. 2016, RvMG, 81, 161
Deienno, R., Izidoro, A., Morbidelli, A., et al. 2018, ApJ, 864, 50
Deienno, R., Izidoro, A., Morbidelli, A., Nesvorny, D., & Bottke, W. F. 2022, ApJL, 936, L24
Delbo', M., Walsh, K., Bolin, B., Avdellidou, C., & Morbidelli, A. 2017, Sci, 357, 1026
Diamond-Lowe, H., Kreidberg, L., Harman, C. E., et al. 2022, arXiv:2207.12755
Dorn, C., & Lichtenberg, T. 2021, ApJL, 922, L4
Doyle, A. E., Desch, S. J., & Young, E. D. 2021, ApJL, 907, L35
Dressing, C. D., & Charbonneau, D. 2015, ApJ, 807, 45
Drążkowska, J., & Alibert, Y. 2017, A&A, 608, A92
Drążkowska, J., Bitsch, B., Lambrechts, M., et al. 2022, arXiv:2203.09759
Drążkowska, J., & Dullemond, C. P. 2018, A&A, 614, A62
Elkins-Tanton, L. T., & Seager, S. 2008a, ApJ, 688, 628
Elkins-Tanton, L. T., & Seager, S. 2008b, ApJ, 685, 1237
Evans, A. J., Andrews-Hanna, J. C., Head, J. W., et al. 2018, JGRE, 123, 1596
Feng, F., Butler, R. P., Shectman, S. A., et al. 2020, ApJS, 246, 11
Ferus, M., Rimmer, P., Cassone, G., et al. 2020, AsBio, 20, 1476
Fischer-Gödde, M., & Kleine, T. 2017, Natur, 541, 525
Fulton, B. J., Petigura, E. A., Howard, A. W., et al. 2017, AJ, 154, 109
Gaidos, E., Mann, A. W., Kraus, A. L., & Ireland, M. 2016, MNRAS, 457, 2877
Gaillard, F., Bouhifd, M. A., Füri, E., et al. 2021, SSRv, 217, 22
Gaudi, B. S., Seager, S., Mennesson, B., et al. 2020, arXiv:2001.06683
Genda, H., Brasser, R., & Mojzsis, S. J. 2017a, E&PSL, 480, 25
Genda, H., Iizuka, T., Sasaki, T., Ueno, Y., & Ikoma, M. 2017b, E&PSL, 470, 87
Genda, H. 2019, in Astrobiology, ed. A. Yamagishi, T. Kakegawa, & T. Usui (Berlin: Springer), 197
Gilbert, E. A., Barclay, T., Schlieder, J. E., et al. 2020, AJ, 160, 116
Gillmann, C., Golabek, G. J., Raymond, S. N., et al. 2020, NatGe, 13, 265
Gillon, M., Triaud, A. H. M. J., Demory, B.-O., et al. 2017, Natur, 542, 456
Ginzburg, S., Schlichting, H. E., & Sari, R. 2018, MNRAS, 476, 759
Grimm, R. E., & McSween, H. Y. 1993, Sci, 259, 653
Grimm, S. L., & Stadel, J. G. 2014, ApJ, 796, 23
Halliday, A. N. 2013, GeCoA, 105, 146
Hamano, K., Kawahara, H., Abe, Y., Onishi, M., & Hashimoto, G. L. 2015, ApJ, 806, 216
Hashimoto, G. L., Abe, Y., & Sugita, S. 2007, JGRE, 112, E05010
Hilton, C. D., Ash, R. D., & Walker, R. J. 2022, GeCoA, 318, 112
Hin, R. C., Coath, C. D., Carter, P. J., et al. 2017, Natur, 549, 511
Hirschmann, M. M. 2016, AmMin, 101, 540
Hirschmann, M. M. 2022, GeCoA, 328, 221
Hirschmann, M. M., Bergin, E. A., Blake, G. A., Ciesla, F. J., & Li, J. 2021, PNAS, 118, e2026779118
Huang, D., Badro, J., & Siebert, J. 2020, PNAS, 117, 27893
Ikoma, M., Elkins-Tanton, L., Hamano, K., & Suckale, J. 2018, SSRv, 214, 76
Itcovitz, J. P., Rae, A. S. P., Citron, R. I., et al. 2022, PSJ, 3, 115
Jin, Z., & Bose, M. 2019, SciA, 5, eaav8106
Jin, Z., Bose, M., Lichtenberg, T., & Mulders, G. D. 2021, PSJ, 2, 244
Johansen, A., Mac Low, M.-M., Lacerda, P., & Bizzarro, M. 2015, SciA, 1, 1500109
Jontof-Hutter, D. 2019, AREPS, 47, 141
Kendall, J. D., & Melosh, H. J. 2016, E&PSL, 448, 24
Kitadai, N., & Maruyama, S. 2018, Geosci. Front., 9, 1117
Kleine, T., & Walker, R. J. 2017, AREPS, 45, 389
Kopparapu, R. K., Ramirez, R., Kasting, J. F., et al. 2013, ApJ, 765, 131
Korenaga, J. 2021, PreR, 359, 106178
Kral, Q., Wyatt, M. C., Triaud, A. H. M. J., et al. 2018, MNRAS, 479, 2649
Krijt, S., Kama, M., McClure, M., et al. 2022, arXiv:2203.10056
Krissansen-Totton, J., Fortney, J. J., Nimmo, F., & Wogan, N. 2021, AGUA, 2, e00294
Kurokawa, H., Shibuya, T., Sekine, Y., et al. 2022, AGUA, 3, e00568
Kuwahara, H., & Sugita, S. 2015, Icar, 257, 290
Lam, K. W. F., Csizmadia, S., Astudillo-Defru, N., et al. 2021, Sci, 374, 1271
Lammer, H., Zerkle, A. L., Gebauer, S., et al. 2018, A&ARv, 26, 2
Lewis, J. A., & Jones, R. H. 2016, M&PS, 51, 1886
Li, R., Youdin, A. N., & Simon, J. B. 2019, ApJ, 885, 69
Lichtenberg, T. 2021, ApJL, 914, L4
Lichtenberg, T., Bower, D. J., Hammond, M., et al. 2021a, JGRE, 126, e06711
Lichtenberg, T., Drążkowska, J., Schönbächler, M., Golabek, G. J., & Hands, T. O. 2021b, Sci, 371, 365
Lichtenberg, T., Golabek, G. J., Burn, R., et al. 2019, NatAs, 3, 307
Lichtenberg, T., & Krijt, S. 2021, ApJL, 913, L20
Lichtenberg, T., Schaefer, L. K., Nakajima, M., & Fischer, R. A. 2022, arXiv:2203.10023
Liggins, P., Jordan, S., Rimmer, P. B., & Shorttle, O. 2022, JGRE, 127, e07123
Liggins, P., Shorttle, O., & Rimmer, P. B. 2020, E&PSL, 550, 116546
Luger, R., & Barnes, R. 2015, AsBio, 15, 119
Luque, R., & Palle, E. 2022, Sci, 377, 1211
Massol, H., Hamano, K., Tian, F., et al. 2016, SSRv, 205, 153
Medina, A. A., Winters, J. G., Irwin, J. M., & Charbonneau, D. 2022, ApJ, 935, 104
Miguel, Y., Guilera, O. M., & Brunini, A. 2011, MNRAS, 417, 314
Miotello, A., Kamp, I., Birnstiel, T., Cleeves, L. I., & Kataoka, A. 2022, arXiv:2203.09818
Mojzsis, S. J. 2021, arXiv:2112.04309
Mojzsis, S. J., Brasser, R., Kelly, N. M., Abramov, O., & Werner, S. C. 2019, ApJ, 881, 44
Morbidelli, A., Bottke, W. F., Nesvorný, D., & Levison, H. F. 2009, Icar, 204, 558
Nesvorný, D., & Morbidelli, A. 2012, AJ, 144, 117
Nesvorný, D., Roig, F. V., & Deienno, R. 2021, AJ, 161, 50
Norris, C. A., & Wood, B. J. 2017, Natur, 549, 507
O'Brien, D. P., Izidoro, A., Jacobson, S. A., Raymond, S. N., & Rubie, D. C. 2018, SSRv, 214, 47
Öberg, K. I., & Bergin, E. A. 2021, PhR, 893, 1
Ogihara, M., & Ida, S. 2009, ApJ, 699, 824
Owen, J. E., Shaikhislamov, I. F., Lammer, H., Fossati, L., & Khodachenko, M. L. 2020, SSRv, 216, 129
Owen, J. E., & Wu, Y. 2017, ApJ, 847, 29
Paschek, K., Kohler, K., Pearce, B. K. D., et al. 2022, arXiv:2204.06523
Paschek, K., Semenov, D. A., Pearce, B. K. D., et al. 2021, arXiv:2112.09160
Pearce, B. K. D., Tupper, A. S., Pudritz, R. E., & Higgs, P. G. 2018, AsBio, 18, 343
Peslier, A. H., Schönbächler, M., Busemann, H., & Karato, S.-I. 2017, SSRv, 212, 743
Piani, L., Marrocchi, Y., Rigaudier, T., et al. 2020, Sci, 369, 1110
Pierrehumbert, R. T., & Hammond, M. 2019, AnRFM, 51, 275
Pordes, R., Petravick, D., Kramer, B., et al. 2007, JPhCS, 78, 012057
Quanz, S. P., Ottiger, M., Fontanet, E., et al. 2022, A&A, 664, A21
Quintana, E. V., Barclay, T., Borucki, W. J., Rowe, J. F., & Chambers, J. E. 2016, ApJ, 821, 126
Raddi, R., Gansicke, B. T., Koester, D., et al. 2015, MNRAS, 450, 2083
Raymond, S. N., & Izidoro, A. 2017, Icar, 297, 134
Raymond, S. N., Izidoro, A., Bolmont, E., et al. 2022, NatAs, 6, 80
Raymond, S. N., Izidoro, A., & Morbidelli, A. 2020, in Planetary Astrobiology, ed. V. S. Meadows et al. (Tucson, AZ: Univ. of Arizona Press), 287
Raymond, S. N., O'Brien, D. P., Morbidelli, A., & Kaib, N. A. 2009, Icar, 203, 644
Raymond, S. N., Scalo, J., & Meadows, V. S. 2007, ApJ, 669, 606
Raymond, S. N., Schlichting, H. E., Hersant, F., & Selsis, F. 2013, Icar, 226, 671

Rein, H., & Tamayo, D. 2015, MNRAS, 452, 376
Rimmer, P. B., Ferus, M., Waldmann, I. P., et al. 2020, ApJ, 888, 21
Rimmer, P. B., Majumdar, L., Priyadarshi, A., Wright, S., & Yurchenko, S. N. 2021, ApJL, 921, L28
Rodriguez, J. E., Vanderburg, A., Zieba, S., et al. 2020, AJ, 160, 117
Rogers, J. G., & Owen, J. E. 2021, MNRAS, 503, 1526
Rollinson, H., Adetunji, J., Lenaz, D., & Szilas, K. 2017, Litho, 282, 316
Rubie, D. C., Jacobson, S. A., Morbidelli, A., et al. 2015, Icar, 248, 89
Salvador, A., Massol, H., Davaille, A., et al. 2017, JGRE, 122, 1458
Sarafian, A. R., Hauri, E. H., McCubbin, F. M., et al. 2017, RSPTA, 375, 20160209
Sasselov, D. D., Grotzinger, J. P., & Sutherland, J. D. 2020, SciA, 6, eaax3419
Sasselov, D. D., & Lecar, M. 2000, ApJ, 528, 995
Scalo, J., Kaltenegger, L., Segura, A., et al. 2007, AsBio, 7, 85
Schaefer, L., & Fegley, B. J. 2017, ApJ, 843, 120
Schaefer, L., Wordsworth, R. D., Berta-Thompson, Z., & Sasselov, D. 2016, ApJ, 829, 63
Schlichting, H. E., & Young, E. D. 2022, PSJ, 3, 127
Schoonenberg, D., Liu, B., Ormel, C. W., & Dorn, C. 2019, A&A, 627, A149
Schoonenberg, D., & Ormel, C. W. 2017, A&A, 602, A21
Sekine, Y., Sugita, S., Kadono, T., & Matsui, T. 2003, JGRE, 108, 5070
Sfiligoi, I., Bradley, D. C., Holzman, B., et al. 2009, in The Pilot Way to Grid Resources Using glideinWMS, 2009 WRI World Congress on Computer Science and Information Engineering (New York: IEEE), 428
Siebert, J., Badro, J., Antonangeli, D., & Ryerson, F. J. 2013, Sci, 339, 1194
Sinclair, C. A., Wyatt, M. C., Morbidelli, A., & Nesvorný, D. 2020, MNRAS, 499, 5334
Stagno, V., & Aulbach, S. 2021, Magma Redox Geochemistry, Vol. 19 (Washington, DC: American Geophysical Union)
Stephant, A., Wadhwa, M., Hervig, R., et al. 2021, GeCoA, 297, 203
Suárez Mascareño, A., Faria, J. P., Figueira, P., et al. 2020, A&A, 639, A77
Tian, F., & Ida, S. 2015, NatGe, 8, 177
Todd, Z. R., & Oberg, K. I. 2020, AsBio, 20, 1109
Trail, D., Bruce Watson, E., & Tailby, N. D. 2012, GeCoA, 97, 70
Turbet, M., Ehrenreich, D., Lovis, C., Bolmont, E., & Fauchez, T. 2019, A&A, 628, A12
Unterborn, C. T., Desch, S. J., Hinkel, N. R., & Lorenzo, A. 2018, NatAs, 2, 297
Venturini, J., Guilera, O. M., Haldemann, J., Ronco, M. P., & Mordasini, C. 2020a, A&A, 643, L1
Venturini, J., Ronco, M. P., & Guilera, O. M. 2020b, SSRv, 216, 86
Wang, H. S., Lineweaver, C. H., & Ireland, T. R. 2019a, Icar, 328, 287
Wang, H. S., Liu, F., Ireland, T. R., et al. 2019b, MNRAS, 482, 2222
Wolfe, J. M., & Fournier, G. P. 2018, Nat. Ecol. Evol, 2, 897
Woo, J. M. Y., Grimm, S., Brasser, R., & Stadel, J. 2021, Icar, 359, 114305
Wordsworth, R., & Kreidberg, L. 2022, ARA&A, 60, 159
Wordsworth, R. D., Schaefer, L. K., & Fischer, R. A. 2018, AJ, 155, 195
Wyatt, M. 2020, in The Trans-Neptunian Solar System, ed. D. Prialnik, M. A. Barucci, & L. Young (Amsterdam: Elsevier), 351
Yoshida, T., & Kuramoto, K. 2021, MNRAS, 505, 2941
Young, E. D., Shahar, A., Nimmo, F., et al. 2019, Icar, 323, 1
Zahnle, K. J., & Carlson, R. W. 2020, in Planetary Astrobiology, ed. V. S. Meadows et al. (Tucson, AZ: Univ. of Arizona Press), 3
Zahnle, K. J., Lupu, R., Catling, D. C., & Wogan, N. 2020, PSJ, 1, 11